Finite element modeling of porous polymer pipeline coating using X-ray micro computed tomography

Ole Vestrum [a,b,*], Magnus Langseth [a,b], Tore Børvik [a,b]

[a] Structural Impact Laboratory (SIMLab), Department of Structural Engineering, Norwegian University of Science and Technology (NTNU), NO-7491, Trondheim, Norway
[b] Centre for Advanced Structural Analysis (CASA), NTNU, NO-7491, Trondheim, Norway

ARTICLE INFO

ABSTRACT

Offshore pipelines are designed to sustain impact from fish trawl equipment and anchors, but due to component complexity, insulating coating solutions are often neglected in mechanical capacity estimates. In this work, efforts are made to predict the mechanical behavior of a typical polymeric insulating coating solution using the finite element method. To do so, the multi-scale morphology of porous polymer coating specimens was mapped using X-ray Micro Computed Tomography (XRMCT) and Differential Scanning Calorimetry (DSC). XRMCT-based finite element models were then derived, analyzed and evaluated against compression tests and the DSC results. The modeling approach produced good correspondence with experimental tests.

1. Introduction

Rigid steel pipelines are used to transport bore fluids extracted from subsea oil and gas reservoirs along the seabed. During this extraction process, it is beneficial to conserve a high fluid temperature to prevent the formation of hydrocarbon precipitates and loss of pressure. A utilized passive solution is to insulate the outer surface of the pipeline from the low temperature of the ambient seawater. Multi-layer polymeric coating systems are often applied as insulation due to the resilience of certain polymers to the harsh conditions found in such environments. The insulting properties are ascribed to the relatively thick-foamed layers, which are part of the full coating solutions. The foaming process creates small pores of various shape, size and orientation where gas is trapped as the polymeric material solidifies during production. While residing on the seabed, pipelines are also at the risk of impacts from anchors and trawl gears [1]. The primary purpose of the insulating coatings is to prevent the loss of heat, but such solutions are also experienced to absorb a significant amount of energy during impact events [2]. In fact, cellular structures are much used to mitigate impact loads in other applications [3]. According to the prevailing standard for pipeline design [4], the beneficial mechanical effects of coating systems may be included in the design evaluation of subsea pipelines if their respective effectiveness are documented. The crash worthiness of a pipeline design may be proven through either experimental tests or computational analyses. The cost-effectiveness and versatility of numerical estimates often make them a preferred choice when evaluating mechanical designs. However, the complex nature of many insulating coatings inhibits their impact mitigating effect to be estimated using numerical approaches like the finite element method (FEM).

Over the last couple of decades, X-ray micro computed tomography (XRMCT) has been used to derive finite element meshes of the actual morphology in cellular materials [5,6,33]. Elliott et al. [7] studied the deformation mechanisms of an open-cell polyurethane foam with XRMCT under a range of compressive strains, and attempted to derive node-strut models of the undeformed morphology. The authors found the scans to be in good agreement with the corresponding SEM micrographs, but they were unable to establish a working finite element model. Youssef et al. [8] utilized XRMCT to map the internal pore structure of a single 6 mm diameter cylindrical polyurethane foam specimen (with a 33% density relative to that of solid polyurethane) at various stages of a compression test. A scan of the initial internal morphology was used to build volumetric tetrahedral meshes at various resolutions, which was used in subsequent finite element analyses. The numerical kinematics and force reactions were compared to the experimental data with good results. XRMCT has also been used to create statistical descriptions of materials, and these statistics were applied to

construct finite element models. This was done by e.g. Dastgerdi et al. [9] when studying the effect of clustering in particulate composite materials. In addition to foams, XRMCT has also been used in the study of other engineering materials and structures like cellular ceramics [10] cement paste [11], fiber-reinforced polymers [12,13] and foam-core sandwich panels [14]. Vestrum et al. [2] used XRMCT to gather information of the porous morphology of a pipeline coating material.

There exists a great economic potential in allowing polymeric insulating solutions to serve also as structural components when assessing the integrity of subsea pipelines under various impact loading situations. Numerical models are both cost-effective and versatile alternatives to loading-specific large-scale experimental component tests. However, coating designs with advanced engineering materials complicate the use of standard numerical modeling approaches in assessing different products' contributions to the mechanical response of a full pipeline. Earlier studies [2,15] have revealed a highly inhomogeneous porous structure, causing a distinct variation in mechanical behavior across the thickness of typical foamed coating systems. Techniques that are more sophisticated must therefore be investigated in order to incorporate porous coating systems into mechanical assessment frameworks. This work aims to establish a numerical modeling methodology using FEM, which may be used in the assessment of the mechanical behavior of porous polymeric pipeline coatings. To this end, XRMCT and Different Scanning Calorimetry (DSC) are used to map a specific polymeric coating product's morphologies at various scales. Finite element meshes are directly derived from the XRMCT scans of cylindrical coating specimens, which are also experimentally tested in compression. The model responses are compared with the experimental results, and improvements are made to the model by evaluating the DSC results. With this work, it is the authors' intent to help find a solution to a yet unresolved engineering problem involving a layered composite structure. XRMCT has proved its use in material sciences during the course of the past few decades. However, while studies employing XRMCT-based models are found in the literature (with the vast majority related to medical applications), few are concerned with investigating ways how these resource-demanding models can be used to derive models which are

more applicable to engineering problems. The novelty of this work lies in the understanding of how advanced XRMCT-based models can be utilized to build continuum-based finite element models to be used in large-scale numerical simulations of real structures. This is done by attempting to isolate the contribution from microscopic (polymer) and macroscopic (porous) material features to the full behavior of the given pipeline coating material.

2. Material

2.1. Porous specimens

The specimens featured in this work are taken from an actual pipeline sample with a multi-layer coating solution applied. While Equinor [16] supplied the full-scale pipeline sample, the coating solution, which is known under the product name Thermotite Polypropylene [17], was produced by Shawcor Norway. Fig. 1 illustrates (a) the full pipeline cross-section with a reference polar coordinate system and (b) a quartile cross-section view with radial measurements of the various layers along with some short descriptions. The reference coordinate system in Fig. 1 (a) is used throughout this study. As seen in Fig. 1(b), the cross-section consists of an inner pipe section made of X65 steel, a 3-layered polypropylene solution (3LPP) in place for corrosion protection and adhesion, a thermally insulating layer of porous polypropylene, and finally an outer shielding layer of a polypropylene material [18]. The latter material is thoroughly characterized by Johnsen et al. [19]. The porous layer is made from a polypropylene block copolymer made by Borealis under the product name BA202E [20], which is mixed with a blowing agent during production. This layer makes up well over 80% of the total coating thickness, and all specimens studied herein were sampled from there. A short description of the coating application reads:

1. A cleaning procedure is performed where corrosion and defects are removed from the steel pipe section through abrasive blasting and surface grinding.
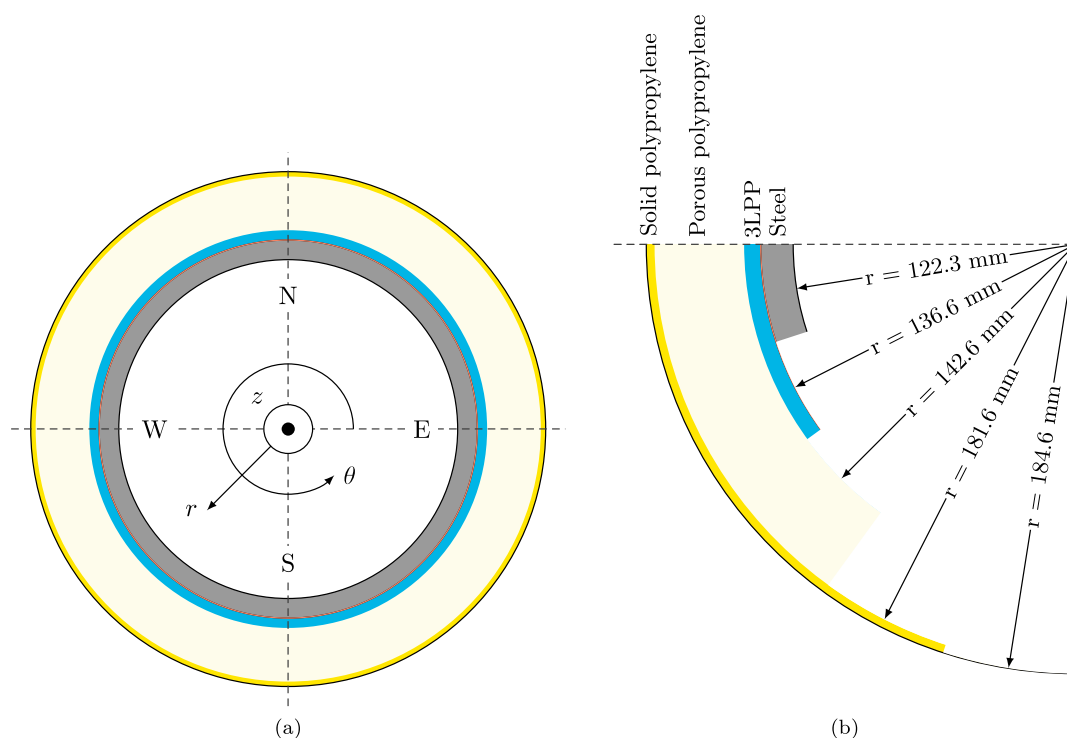

Fig. 1. Illustrations of (a) the full pipeline cross-section and (b) a quartile cross-section view with radial measurements of the various layers relevant to this work.

2. An induction heating process heats the steel to around 220–230 °C, which is followed by a stepwise application of the 3LPP solution. The process can manage 2 m/min.

3. The thermal insulation system is then applied. One thick layer of porous polypropylene and one thin layer of solid polypropylene are extruded at about 200 °C onto the pipeline. The solid layer acts as an outer shield to the ambient seabed environment during operation.

4. After the multi-layer coating has been applied, the pipeline section is quenched by applying water on the outermost layer in order to cool it.

Fifteen cylindrical specimens (three through-thickness cylindrical samples divided into five specimens each) were sampled from a full multi-layer coating slab. The separate positions are indicated in Fig. 2 and given labels **a** to **e**. All specimens had nominal heights and diameters of 6 mm and 10 mm, respectively.

2.2. Solid specimens

In parallel, an 80 mm × 80 mm × 100 mm block of solid BA202E was produced on request by the authors by Shawcor Norway on a separate process line. This block was used to produce six cylindrical test specimens (with the same dimensions as the porous ones) of solid polypropylene. It is noted that different production lines may result in small variation in material characteristics. Thus, the material behavior might not be exactly similar to that of the porous specimens from the pipeline coating system.

3. Experimental work

3.1. X-ray micro computed tomography

XRMCT is a nondestructive technique for obtaining the relative radiodensity variation within three-dimensional bodies. Based on the difference between incident and transmitted X-ray radiation, a series of two-dimensional gray-scale projections of a body are created at different angles. A volume may be reconstructed from these projections using sophisticated software algorithms. The computed volume is represented in a three-dimensional array of cubic voxels assigned an integer value representing the radiodensity at a discrete spatial subspace. For more details regarding the theoretical background of the imaging technique and the various post-processing procedures applied to the collected data sets, the reader is refereed to, e.g., Als-Nielsen and McMorrow [21] and Section 4, respectively.
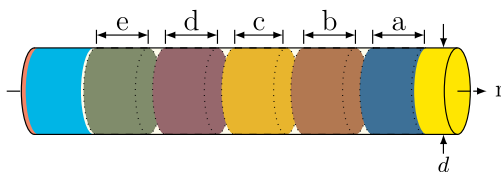
3.1.1. Acquisition

All porous and three randomly selected solid specimens (see Section 2.1 and Section 2.2, respectively) were scanned using XRMCT – where the latter tests were merely intended as a verification to check the absence of voids within the solid specimens. The XRMCT scans were acquired using a Nikon XT H225 ST MicroCT machine located at the Norwegian University of Science and Technology (NTNU). This machine is an X-ray tube-based device, which produces a conical beam of polychromatic X-rays. All scans were made with a 225 kV wolfram reflection target and a panel detector with 2000 × 2000 pixels, 200 µm pixel size and 16-bit pixel depth. Each tomographic projection was collected using the average of two X-ray images (each with 1 s exposure time) taken at 1571 azimuthal orientations. The volume reconstruction was done using the commercial software Nikon CT Pro 3D (Version XT 3.1.3) and exported as an 8-bit depth gray-scale image stack. Fig. 3 presents examples of surface mesh models rendered with the software of one of scanned porous specimen series.

3.1.2. Results

Fig. 4 presents images at the center cross-section of five porous specimens (originating from the same through-thickness cylindrical sample). The vertical and horizontal dimensions in the images are parallel to the Θ-axis and r-axis in Fig. 1, respectively. A distinct variation in pore morphology along the coating-layer thickness is readily seen – thus giving the specimens a strong macroscopic gradient.

Fig. 5 presents the variation in relative density along the r-axis of the specimens. Shaded areas correspond to the measured average density (measured mass density divided by the mass density of solid polypropylene, i.e., 900 kg/m^3 [20]), for the three specimens at each position including the uncertainty in the utilized weight scale. The solid lines are based on the average gray-value of each cross-sectional image slice with plane normal parallel to the r-axis based on the XRMCT scans of specimens from two out of the three through-thickness cylindrical samples. The different measuring methods are seen to correspond reasonably well with little spread between the comparable specimens. In Gibson and Ashby [3], cellular solids (such as foams) are defined as materials having a relative density below 30%, while the relative density of the porous layer of the investigated coating is seen to vary between 70% and 100% of the density of solid polypropylene. This result suggests that the material at hand is too dense to be modeled using typical constitutive models for foams, but at the same time too porous to be modeled as a solid material. Maire et al. [5] defines such materials as 'porous', a term which is adopted herein.

3.2. Differential Scanning Calorimetry

3.2.1. Microscopic morphology

The full chemical composition of the BA202E material in the porous layer is not known beyond what is stated in the data sheet [20]. However, it is assumed that the microstructure of the polypropylene block copolymer conforms to a semi-crystalline microstructure. Halary et al. [22] describe a typical semi-crystalline polymer as consisting of rigid crystalline regions dispersed in a more or less disordered amorphous phase. It is also stated that rapid cooling of a polymer melt influences the formation of crystals, as the polymeric chains are unable to pack into more tightly packed regions. As detailed in Section 2, one of the final

Fig. 2. Through-thickness cylindrical coating sample with specimen origins and associated labels.

Fig. 3. 3D rendering of the XRMCT data sets of one of the porous specimen series (specimens with origin **e** to **a** are printed from left to right, respectively).
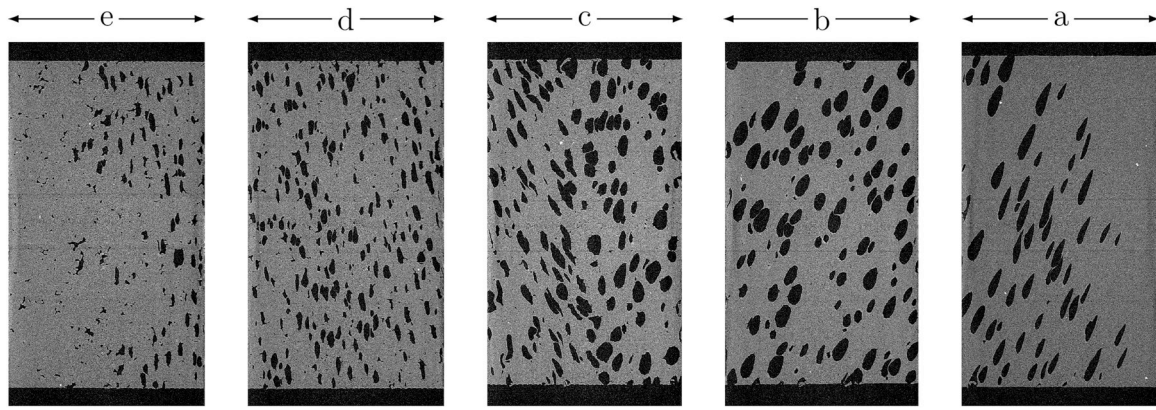
Fig. 4. XRMCT images of the vertical cross-sections (with the out-of-plane normal parallel to the *z*-axis) of a set of porous cylindrical specimens. The labels correspond to the positions indicated in Fig. 1.
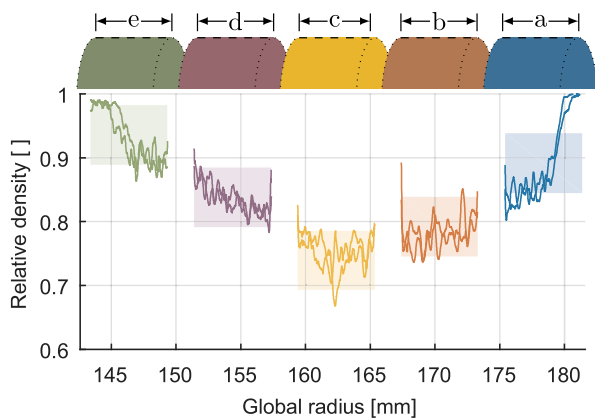

Fig. 5. Relative densities in the specimens based on measured average densities (shaded areas) and radiodensities from XRMCT (solid lines).

steps in the production procedure of the multi-layer coating system is to quench the external pipeline surface (i.e., the coating surface) by applying water. This will inevitably induce a gradient in the temperature rate throughout the coating layers during transient cooling. It is therefore presumed that there exists a variation in the microstructure across the layer thickness [31]. Doroudiani et al. [23] studied the effect of crystallinity in a foamed structure using different semi-crystalline polymers, including polypropylene. The different crystalline structures were developed by differing the cooling rate during production. As the solubility and diffusivity of CO_2 gas (as produced during the foaming processes) in the polymer matrix is a function of the crystallinity, this phenomenon also influenced the resulting porous structure. This is argued to be because the absorption and diffusion occurs mainly in the amorphous regions [24].

3.2.2. Setup

DSC is a common thermo-analytical technique used to characterize several key features of a semi-crystalline polymer specimen [22] – such as the degree of crystallinity within the bulk material. A series of DSC tests on specimens retrieved throughout the coating thickness was performed to document a potential variation in the microstructural features. The experimental program included tests on material from 5 different positions with 3 repetitions at each position, i.e., 15 tests in total. The samples were approximately 3 mm × 3 mm × 1 mm in size. All tests were performed using a double-furnace DSC 8500 from PerkinElmer with nitrogen at 1 atm as inert atmosphere and a heating rate of 10 °C/min starting from 20 °C and ending at 200 °C. To establish a baseline for the crystallinity calculations, a test program was also run

with an empty pan. The melt enthalpies was automatically integrated by the PerkinElmer software.

3.2.3. Results

Fig. 6 shows the results from the DSC tests. The black markers give the average of the 3 repetitions at each location, while the red vertical error bars represent the spread. A heat of fusion value of 207 J/g is used as reference to create the values in the plot. This value corresponds to that of a hypothetical 100% crystalline polypropylene material, so the actual percentage obtained has some uncertainty. However, the heat needed for melting the material is found to be a distinct function of the *r*-axis, which may be accredited to microscopic differences throughout the polymeric layer. It is likely that this, in turn, will influence the mechanical behavior of the material.

3.3. Compression tests

A quasi-static uniaxial compression test program was conducted in the following to map the mechanical response of both the 15 specimens from the porous coating and the 6 specimens from the solid block of polypropylene.

3.3.1. Setup

All compression tests were performed in an Instron 5982-L2035 universal test machine [25] with an Instron 2580–301 (100 kN) load cell used to record the reaction force (F) during testing. According to the datasheet of the load cell, an uncertainty of ±0.15% in force measurements are to be expected at the achieved force levels. The air humidity and the room temperature were measured to be in the intervals of 26–28% and 22–25 °C, respectively, during the testing period. A
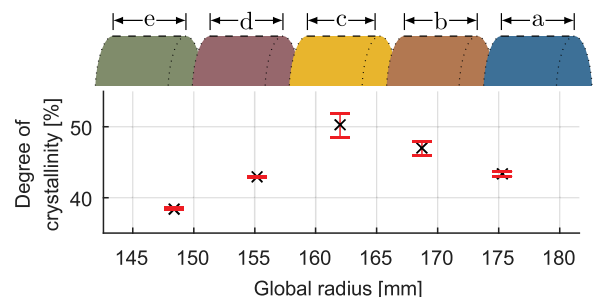

Fig. 6. Variation in material crystallinity across the coating thickness from DSC analyses with a reference enthalpy of fusion of 207 J/g. The black markers and the red error bars show the average and maximum spread, respectively, based on 3 repetitions at equal location. (For interpretation of the references to color in this figure legend, the reader is referred to the Web version of this article.)

multi-purpose lubrication was applied to both ends of the cylindrical specimens as a means to minimize friction between the rigid platens of the test machine and the specimen. A 5-megapixel Prosilica GC2450 camera was used to capture the deformation sequence, which was synchronized with the crosshead displacement (Δ) of the test machine and the force output. Fig. 7 shows one of the solid specimens at various deformations during testing. The blue and red illustrative lines are results from a software routine used for tracing the peripheral side edges of the specimens. These are used to estimate the evolution of the cross-section area (A) of the specimen during testing. In addition, all specimens were painted with a black and white speckle pattern to enable the retrieval of strain fields at the specimens' surfaces through digital image correlation (DIC) analyses – even though this was not utilized in the work presented herein. However, by using subset tracking (available in the in-house DIC software eCorr [26]) of a checkerboard pattern mounted near the interface of the test machine and the specimen, a maximum error estimate below 2% for the machine displacement at maximum force was obtained. The machine crosshead displacement was therefore deemed adequate as a displacement measure. The deformation rate was set to 0.006 mm/s to achieve quasi-static conditions.

From the stated measurements, the Cauchy stress σ and the logarithmic strain ε could be calculated as $\sigma = F/A$ and $\varepsilon = \ln(1 + \Delta/h)$, where h is the initial height of the specimens. However, a caveat is made towards deriving and utilizing this kind of material data from such highly inhomogeneous specimens. Due to the graded material features across the specimens' height, the stress distribution will not be uniform and therefore likely result in strain localization at early stages of the deformation. This inhomogeneous violates essential requirements for proper material characterization. While these mechanical tests may not strictly fulfill the conditions of material tests, their viability as component tests is still justified.

3.3.2. Results

Fig. 8(a) presents raw force-displacement curves recorded during testing, while post-processed Cauchy stress-logarithmic strain curves for all tests are plotted in Fig. 8(b). While the repeatability between specimens of the same spatial origin is good, a distinct spread across the *r*-axis in terms of mechanical response is seen. Not surprisingly, the solid specimens yield the highest stress response. The regions close to the layer edges (**e** and **a**) are seen to produce a higher force response than the intermediate regions, at least up to a displacement of around 2 mm. These regions are according to Fig. 5 known to be the areas with the highest densities. The specimens originating from the midmost region **c** are seen to have the lowest force response during initial stages of compression. This region is also found to have the lowest density throughout the thickness of the coating layer. An interesting crossover behavior is observed for the **b** and **d** specimens followed by a distinct **a/d** and **b/c** grouping at displacements above 2 mm. As the specimens becomes compressed, the pore volume fraction will shrink. It is reasoned that at some point during compression, the mechanical behavior will tend to that of the solid polypropylene material as the specimen densifies at large strains.

The measured elastic stiffness modulus and the tangent modulus (defined in Fig. 9(a)) for the porous specimens' data in Fig. 8(b) are presented in Fig. 9(b). The latter tangent is reasoned to give an indication of the actual tangent modulus of the polymeric material. The lowest initial stiffness is observed in the specimens sampled from region **c**, which is expected as this is the least dense part of the coating layer, and the elastic stiffness of cellular materials is known to decrease with decreasing density [3]. However, a discrepancy is observed between the specimens sampled in regions **b** and **d**. The latter region has the highest measured density of the two, but appears to have the lowest initial stiffness. However, Fig. 6 gives indications that this region also has less crystalline structure. It is also noticed that the shape of variation in the densification tangent modulus show a clear resemblance to the variation in crystallinity presented in Section 3.2.3.

4. Numerical work

4.1. XRMCT-based modeling

4.1.1. Preliminary

An image may be considered as a depiction of geometrical features using some sort of imaging technique. The notion of using depictions in deriving finite element models, which closely mirrors actual geometrical shapes, dates back decades [5,8]. Adopting XRMCT as the imaging
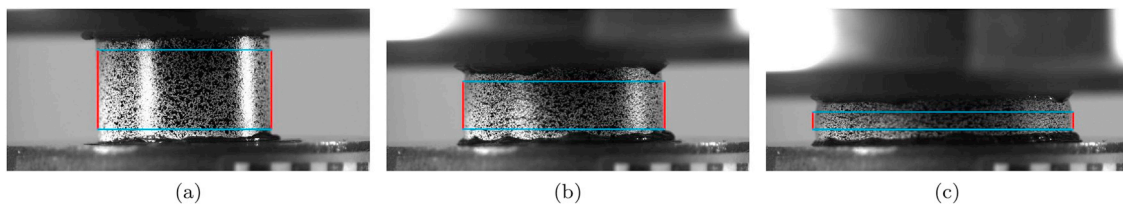

Fig. 7. Still images of a solid specimen during compression at (a) 0.0 mm, (b) 1.8 mm and (c) 3.5 mm deformation.
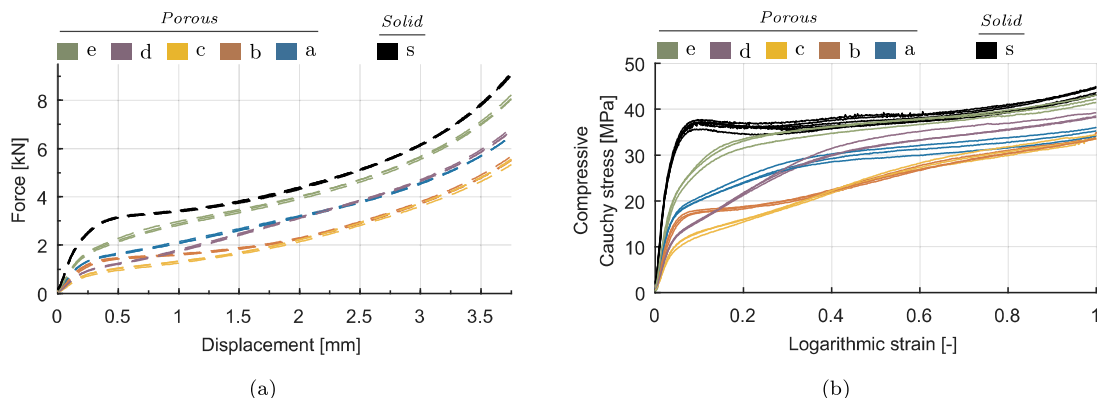

Fig. 8. Results from the uniaxial compression tests with (a) raw force-displacement curves and (b) post-processed Cauchy stress-logarithmic strain curves.
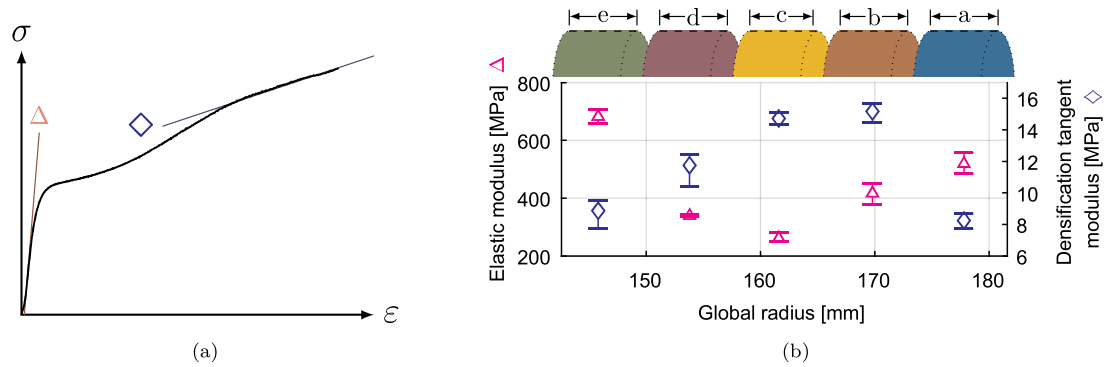
Fig. 9. Variation in elastic and densification tangent moduli from the true stress-strain data in Fig. 8(b). Figure (a) indicates the positions of the tangents while figure (b) gives the variation. The markers indicate the average values while the error bars presents the maximum spread between repetitions.

method, the attenuation of X-ray radiation across a volume is used to depict mass present within the respective space. As the amount of radiation attenuated differs between different materials, an image of the volume depicting the (relative) radiodensities is collected. While traditional modeling often entails significant simplifications of the geometry, XRMCT-based models are often highly resolute to resemble geometrical features accurately. This results in large systems requiring considerable computational resources, thus becoming generally impractical for engineering purposes. However, as computational availability and power are seemingly ever-increasing, XRMCT-based modeling is becoming more and more applicable. This is especially relevant in applications where heterogeneous materials (such as composite or polycrystalline materials) are used. For such cases, the homogenization of material characteristics when developing material models is challenging. A traditional approach is to derive specific properties of a multiphase material based on the respective properties and portions of its constituents through some kind of scaling law. Examples are to use the volume fractions of fibers and matrix (with their individual responses) to estimate their combined behavior in fiber-reinforced materials [13] or to scale the behavior of completely dense solid when working with cellular materials [3]. However, such scaling laws say nothing about the architecture of the material. If comparing the densities of the specimens used herein (Fig. 5) with the corresponding stress-strain response (Fig. 8(b)), it becomes obvious that a simple scaling law would not be sufficient in modeling the mechanical behavior under large deformations.

The literature on XRMCT-based modeling of cellular materials is extensive, and Maire et al. [5] provide a comprehensive overview of the subject matter. The authors identify three classes of developing meshes from tomographic images:

1. Meshes of beam- or plate elements generated from vertex/face information: This class segments vertices and faces in an image of rather thin-walled cellular architectures (such as low-density foams) to build meshes consisting of one- and two-dimensional elements.
2. Meshes of solid hexahedral elements generated from voxel information: This class translates density information from each voxel into a structured hexahedral (cubic) element mesh.
3. Meshes of solid tetrahedral elements generated from surface information: This class creates an unstructured tetrahedral element mesh in the volume contained between the surfaces of segmented phases.

As the first class is more appropriate for thin-wall morphologies (such as foams), the two latter classes are more relevant for the structural features in the porous material studied herein. Ulrich et al. [27] compared meshes pertaining to the second and third classes produced from scans of human trabecular bones. It was concluded that hexahedral element meshes produced excellent analysis results for bones with large trabecular thicknesses, while thinner trabecular structures required

tetrahedral meshes to preserve geometry and connectivity. The tetrahedral type of meshes are found to be more accurate, but demanded much larger computational resources and algorithms that are more complex. Thus, due to the ease of implementation and the rather dense material topology, the modeling approach presented in the following belong under the second type of class with sub-resolution [5].

4.1.2. Mesh derivation

The radiodensity of a body is a measure of its opacity to radiation pertaining to certain parts of the electromagnetic spectrum (including X-ray waves). Let the radiodensity of a three-dimensional volume be represented by the continuous function ρ so that

$$\rho = \rho(\boldsymbol{x}), \boldsymbol{x} \in \mathbb{R}^3$$

where $\boldsymbol{x}$ denotes a spatial point within a volume. In XRMCT, a given scanned volume is discretized into a three-dimensional array of structured cubic (hexagonal) subspaces – called voxels (analogous to the two-dimensional pixels of a digital photography). The radiodensity of each individual voxel is represented on a discrete scale between black and white (i.e., a gray-scale). Both the discretization into voxels and the discretization of the gray-scale are attributed to the pixel resolution and depth of the XRMCT detector assembly. Herein, the three-dimensional discrete scalar field containing the gray-values of all voxels is denoted $\boldsymbol{\rho}$ – with its domain and range governed by the voxel and gray-scale discretizations, respectively.

a) In this work, $\boldsymbol{\rho}$ may explicitly be formulated as

$$\boldsymbol{\rho} \in \{0, 1, 2, \ldots, 253, 254, 255\}^{2000 \times 2000 \times 2000}$$

where the range limits 0 and 255 correspond to a fully radiolucent and a fully radiodense material point, respectively. While the detector device was capable of 16-bit pixel depth, only 8-bit pixel depth was utilized to reduce space and computational demands. In Fig. 10 (a), a two-dimensional visual representation of a cross-section slice of $\boldsymbol{\rho}$ from one of the cylindrical specimens is presented. Fully black and fully white pixels in the cross-section image corresponds to gray-scale values of 0 and 255.

b) As noise and artifacts are often accumulated during XRMCT, $\boldsymbol{\rho}$ needs to be low-pass filtered to smooth out certain high frequencies in the three-dimensional image – and facilitate subsequent steps. This involves taking the convolution between $\boldsymbol{\rho}$ and a filter kernel $\mathbf{g}$ to establish the filtered scalar field $\tilde{\boldsymbol{\rho}}$, i.e.,

$$\tilde{\boldsymbol{\rho}} = \boldsymbol{\rho} * \mathbf{g}$$

In the models produced herein, a bilateral filtering scheme [28] was employed. The bilateral filter is a combination of domain and range
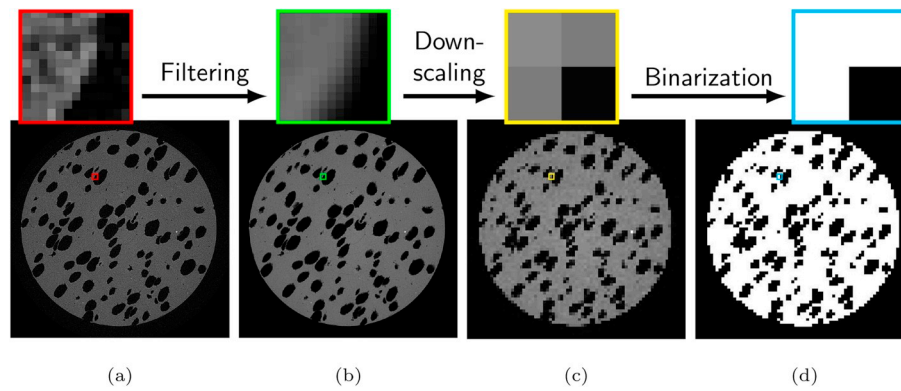
Fig. 10. Post-processing route for mesh derivation from (a) raw, to (b) filtered, to (c) downscaled and finally to (d) binarized radiodensity measurements.

filtering. The Euclidean distances of a given element in ρ and its neighbors in space (domain) and gray-scale value (range) are used to derived the corresponding (and filtered) element in $\tilde{\rho}$. Gaussian functions are used in this study to establish how large weight a neighbor should have as a function of these distances. Thus, each element is filtered based on both its neighbors' spatial closeness and gray-value similarity. This scheme is ideal for preserving edges [28], which is essential when establishing a clear distinction between matter and pore. Fig. 10(b) illustrates a cross-section slice of $\tilde{\rho}$, which has been filtered using the described filtering bilateral scheme.

c) As the radiodensity mappings are to be used as the base in developing a finite element mesh representing the specimen morphology, a resolution of 8.0e9 (2000^3) hexagonal voxels is infeasible, and must therefore be reduced. Such a downscaling operation will inevitably result in loss of geometrical features in the pore morphology, but is essential as it will govern to the amount of elements in the final finite element model. To this end, a Nearest-Neighbor interpolation scheme was used to establish a low-resolution version of $\tilde{\rho}$, denoted $\check{\rho}$. Fig. 10(c) shows the outcome of a downscaling of $\tilde{\rho}$ by a factor of around 25 (in all three dimensions), which resulted in $\check{\rho}$ with a domain of $80 \times 80 \times 80$ voxels, and voxels with 0.15 mm large sides. Overall, the choice of scaling factor is a question of computational demand versus model accuracy.

d) While the previous step reduced the domain of the scalar field, a reduction of its range is also necessary. As this stepwise procedure aims to distinguish between non-matter and matter, only a binary representation of the gray-scale discretization is needed (i.e., black and white). This basic segmenting operation is known as binarization, which divides the gray-value distribution of $\check{\rho}$ into two classes,

which is stored in $\overline{\rho}$. This is done by identifying a single threshold value ρ_t so that for each element i

$$\overline{\rho}(i) = \begin{cases} 0, \check{\rho}(i) < \rho_t \\ 1, \check{\rho}(i) \geq \rho_t \end{cases}$$

where 0 and 1 correspond to void and polymeric material (or black and white in Fig. 10(d)), respectively. One simple way to determine a suitable threshold value ρ_t is to manually pick a gray-scale value based on observations of the gray-value distribution in $\check{\rho}$. However, there exists other more sophisticated approaches. Otsu's method [29], which was used herein, seeks to find an optimal threshold value ρ_t that minimizes the total spread between the upper and lower parts of the gray-scale histogram by iterating over all possible gray-scale values. This approach requires no manual evaluation of the gray-value distributions.

e) Lastly, the information contained in $\overline{\rho}$ is structured into node and element lists, and stored in an ASCII file readable by Abaqus or any other finite element solver. A finished Abaqus model based on this approach is displayed in Fig. 11.

All steps described above were performed using Python scripting with readily available packages offering open-source implementations of the presented methods.

4.2. Analyses

As the intended purpose of this modeling approach is to enable numerical evaluation of porous pipeline coatings, the previously presented compression tests are used to validate the framework. As observed in
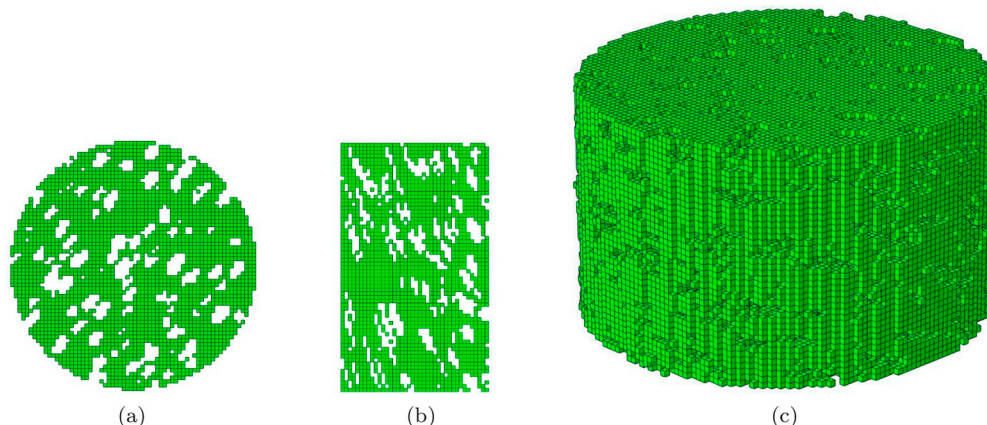

Fig. 11. Cross-sectional views with surface normal parallel to (a) the r-axis, (b) the Θ-axis and (c) an orthographic projection of a hexagonal mesh.
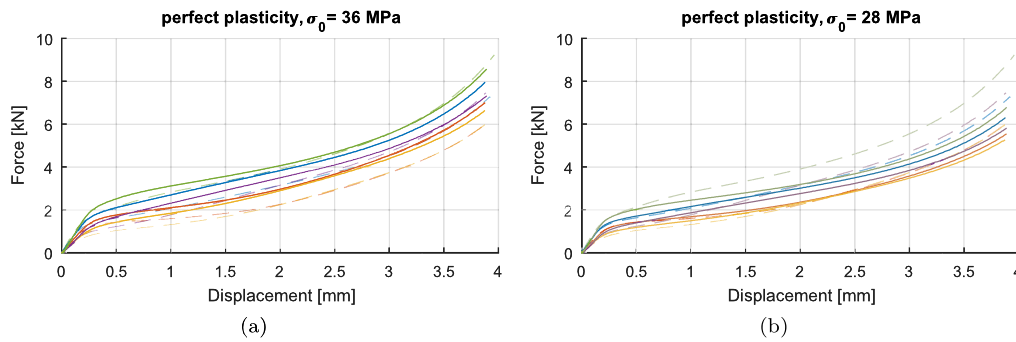
Fig. 12. Results from the hexagonal models (solid lines) using a yield stress of (a) 36 MPa and (b) 28 MPa, respectively, and no work hardening. The corresponding experimental results are also plotted (dashed lines) with the same graph colors for the various specimen positions as defined in Fig. 2. (For interpretation of the references to color in this figure legend, the reader is referred to the Web version of this article.)

Fig. 4, the porous topology varies significantly between the specimens collected at different positions throughout the coating thickness. This allows for inverse calibration of numerical parameters that are shared across a wide range of mesh geometries. In the following analysis series, the XRMCT scans of five specimens from one of the three cylindrical coating sample were used as the bases and compared to the corresponding experimental results. Hexagonal meshes (see Section 4.1.2) were established from XRMCT depictions of the specimens. The meshes used in this study had an element size of 0.08 mm × 0.08 mm × 0.08 mm (giving total element counts between 698870 and 837468), which was found to produce a reasonable balance between analysis run time and representation of the geometrical features. While the spatial discretization of the models account for the macroscopic features of the porous material, the microscopic characteristics of the polypropylene are represented through a material description in the elements. The influence of the constituent material on the global specimen response was therefore also studied by varying the applied material model. Abaqus/Explicit was used for the analyses due to extensive contact and plasticity. In the models, the specimen geometry was placed between two analytical surfaces (representing the rigid platens in the test machine). A velocity was smoothly imposed on the top platen, which compressed the specimen. The velocity was chosen such that the kinetic energy of the model was kept at a reasonable level to avoid inertia effects, while at the same time giving acceptable run times. Linear elements with reduced integration and enhanced hourglass control were applied to the specimens' geometries. If not otherwise stated, all model parameter values (such as friction and elastic parameters) were found through inverse modeling and shared between the five models of each analysis series. Two different friction definitions were used; one for contact between the specimen and the rigid platens using a friction coefficient of 0.02, and one for self-contact within the polypropylene specimen with a friction coefficient equal to 0.1. Linear elasticity with an elastic modulus E of 800 MPa and elastic retraction coefficient ν of 0.4 [30] was also used. The elastic modulus is found to be within reasonable levels when compared to the results from the solid compression tests.

4.2.1. Perfect plasticity

The stress-strain response from the solid polypropylene specimens in Fig. 8(b) exhibit an initial yielding in compression of around 36 MPa with little work hardening. Therefore, a series of simulations including all five specimens with a perfect J_2 plasticity formulation and a yield stress σ_0 of 36 MPa was performed. The employed stress-strain evolution was thus defined as

$$\sigma(\varepsilon) = \begin{cases} E\varepsilon, \varepsilon < \dfrac{\sigma_0}{E} \\ \sigma_0, \varepsilon \geq \dfrac{\sigma_0}{E} \end{cases}$$

Fig. 12(a) illustrates that the hexagonal models with the described material definition in general gave a too high force response when compared with their corresponding experimental results. By lowering the yield stress of the material definition to 28 MPa (as supplied in the BA202E's data sheet), the models correspond well with the experimental data at displacements below 0.5 mm, as presented in Fig. 12(b). The deviations observed at larger deformations may partly be related to the lack of work hardening in the applied model.

4.2.2. Linear hardening

As there exists an obvious variation in the microstructure throughout the thickness of the coating (see e.g. Fig. 6), an analysis scheme where the hardening varies as a function of r may be suitable in order to model the difference in the constituent material behavior. While the degree of crystallinity is known to have a large influence on the mechanical behavior of semi-crystalline polymers, it is not the only microstructural feature affecting the response. The average molecular weight and distribution, along with the size and distribution of crystallites, are also known to have a significant impact. In general, an increased degree of crystallinity is associated with increased stiffness and strength [30,32]. As a means of investigating the significance of such variations, linear isotropic hardening K was added in the following analysis series through the following relation

$$\sigma(\varepsilon) = \begin{cases} E\varepsilon, \varepsilon < \dfrac{\sigma_0}{E} \\ K\left(\varepsilon - \dfrac{\sigma_0}{E}\right), \varepsilon \geq \dfrac{\sigma_0}{E} \end{cases}$$

Based on the variation presented in Fig. 6, attempts were made to vary the value of K as a function r in the specimen models as a way to account for the variation in the microstructure. The K-variation illustrated in Fig. 13 was found to give a very good correspondence with the experimental data, which is presented in Fig. 14(a). All other material variables were kept constant. Apart from the data related to region **e**,
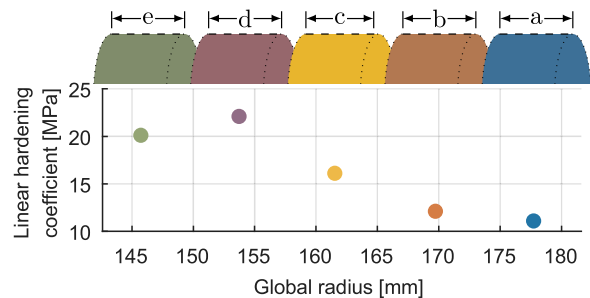

Fig. 13. Established scheme for the through-thickness variation in linear hardening.
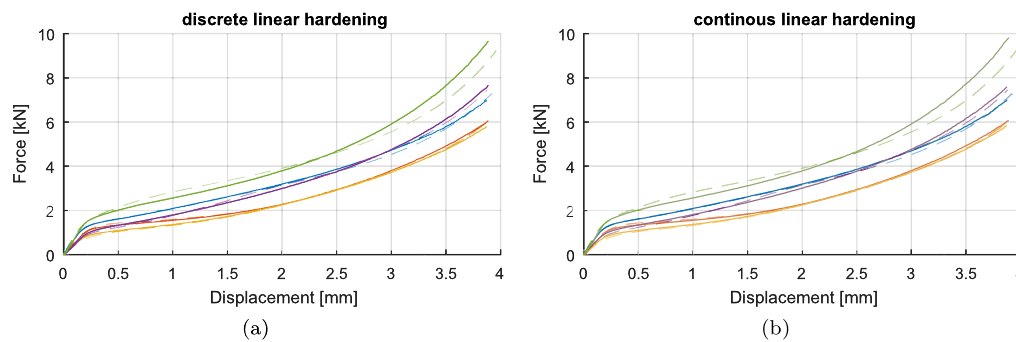
413

Fig. 14. Results from the hexagonal models (solid lines) using (a) discrete and (b) continuous values for the variation in linear hardening coefficient used in the material model. The same line coloring and styling convention as in Fig. 12 are used for these figures.

this simple modification was seen to give a close-to perfect correspondence with the experimental results. One immediate result of including hardening is obvious. While being absent when neglecting hardening, the characteristic grouping and crossover evolution in the force-displacement response between the five specimens are captured when the matrix material is allowed to work harden. In Fig. 14(b), the discrete values from Fig. 13 are interpolated using cubic splines to give a continuous variation to the elements based on their original position along r. This approach gave, essentially, the same results in terms of force-displacement response as the discrete approach, but a continuous variation is more likely. Although the shape of the utilized K-variation is not in perfect correspondence with the variation in degree of crystallinity shown in Fig. 6, comparable convex relationships (as a function of r) are clearly seen between the two.

4.2.3. Other attempts

Several other series of analyses using hexagonal meshes with different modeling features were also examined, but these are excluded as they contributed little or nothing in improving the results. Included in these simulations were:

- Adding isotropic hardening using a power law relation for the matrix material fitted to the stress-strain data between initial yielding and to the point where the tangent stiffness at densifications were retrieved.
- Using linear hardening corresponding to the tangent stiffness at densification as plotted in Fig. 9.
- Adding elements to the pore volumes and applying CO_2 properties via an ideal gas equation of state to the respective (Lagrangian) elements. This resulted in a substantial increase in analysis run time and automatic premature terminations due to the introduction of very low densities and element distortions (due to the low element stiffness). However, the approach was not seen to influence the model response in any other noticeable way up until termination.
- Adding a variation to the elastic modulus as a function of r.

5. Concluding remarks

XRMCT-based voxel models were found to be an excellent starting point in developing finite element models of a porous pipeline coating material. From such models, a low-bound estimate for the compressive behavior of the porous material was established by simply using information provided in the polypropylene data sheet and no evolution of the polymer's yield surface. However, there exists a challenge in more accurate modeling of the polypropylene matrix under large deformations. While the pragmatic augmentation of linear hardening (as a function of the coating thickness) remedied the inconsistencies in force-displacement results at large displacements, the necessary variation in hardening coefficient did not exactly conform to the measured shape of fluctuation in the degree of crystallinity. Future efforts may therefore be focused on developing more sophisticated micromechanical models for

the matrix material. A good understanding of the behavior of the solid phase would nicely complement the XRMCT-based modeling approach in assessing the mechanical response of polymeric pipeline coatings of any design.

As the ultimate goal of this effort is to assess the mechanical behavior of pipelines with porous polymeric coatings under various loading scenarios, further work is needed. Large-scale finite element models usually employ continuum descriptions of the constituent materials in a design. These continuum models represent the homogenized material properties of the volumes confined by the faces of each element. For the coating studied herein, the gradients in both porous architecture and polymeric morphology are seen to have a significant effect on the overall mechanical response. As many advanced engineering applications demand highly discretized element models of the analyzed components, these variations need to be represented at very low length-scales – lower than what is possible through traditional material tests. The work presented herein shows that it is possible to separate the unique contributions produced by both the voids and matrix in such porous polymeric structures. This multi-scale understanding may serve as a valuable approach in establishing continuum material descriptions at much lower length-scales than achievable through mechanical testing.

Acknowledgment

References

[1] The petroleum safety authority Norway. Rørledningsskader – skader og hendelser fra Petroleumstilsynet CODAM database. 2017. Online; accessed, http://www.psa.no/getfile.php/1345620/PDF/Roerledningsskader%20Oktober2017.pdf.

[2] Vestrum O, Kristoffersen M, Polanco-Loria MA, Ilstad H, Langseth M, Børvik T. Quasi-static and dynamic indentation of offshore pipelines with and without multi-layer polymeric coating. Mar Struct 2018;63:60–76. https://doi.org/10.1016/j.marstruc.2018.08.001.

[3] Gibson LJ, Ashby MF. Cellular solids: structures and properties. Cambridge solid state science series. 2. Edition. Cambridge University Press; 1997.

[4] DNV. DNV-OS-F101 submarine pipeline systems. October 2013 [Offshore Standard].

[5] Maire E, Fazekas A, Salvo L, Dendievel R, Youssef S, Cloetens P, Letang JM. X-ray tomography applied to the characterization of cellular materials. Related finite element modeling problems, Composite Science and Technology 2003;63:2431–43.

[6] Maire E, Withers PJ. Quantitative X-ray tomography. Int Mater Rev 2004;59(8): 1–43. https://www.tandfonline.com/doi/full/10.1179/1743280413Y.00000000 23.

[7] Elliott JA, Windle AH, Hobdell JR, Eeckhaut G, Oldman RJ, Ludwig W, Boller E, Cloetens P, Baruchel J. In-situ deformation of an open-cell flexible polyurethane foam characterised by 3D computed microtomography. J Mater Sci 2004;37: 1547–55. https://doi.org/10.1023/A:1014920902712.

[8] Youssef S, Maire E, Gaertner R. Finite element modelling of the actual structure of cellular materials determined by X-ray tomography. Acta Mater 2005;53(3): 719–30. https://doi.org/10.1016/j.actamat.2004.10.024.

[9] Dastgerdi JN, Anbarlooie B, Miettinen A, Hosseini-Toudeshky H, Remes H. Effects of particle clustering on the plastic deformation and damage initiation of particulate reinforced composite utilizing X-ray CT data and finite element modeling. Compos B Eng 2018;153:57–69.

[10] Maire E, Colombo P, Adrien J, Babout L, Biasetto Lisa. Characterization of the morphology of cellular ceramics by 3D image processing of X-ray tomography. J Eur Ceram Soc 2007;27(4):1973–81. https://doi.org/10.1016/j.jeurceramsoc .2006.05.097.

[11] Zhang M, Jivkov AP. Micromechanical modelling of deformation and fracture of hydrating cement paste using X-ray computed tomography characterisation. Compos B Eng 2016;88:64–72. https://doi.org/10.1016/j.compositesb.2015.11.00 7.

[12] Etaati A, Wang H, Pather S, Yan Z, Mehdizadeh SA. 3D X-ray microtomography study on fibre breakage in noil hemp fibre reinforced polypropylene composites. Compos B Eng 2013;50:239–46. https://doi.org/10.1016/j.compositesb.2013.02.0 29.

[13] Notta-Cuvier D, Nciri M, Lauro F, Delille R, Chaari F, Robache F, Haugou G, Maalej Y. Coupled influence of strain rate and heterogeneous fibre orientation on the mechanical behaviour of short-glass-fibre reinforced polypropylene. Mech Mater 2016:186–97.

[14] Rolfe E, Kelly M, Arora H, Hooper PA, Dear JP. Failure analysis using X-ray computed tomography of composite sandwich panels subjected to full-scale blast loading. Compos B Eng 2017;129:26–40.

[15] Hegdal JP, Tofteberg TR, Schjelderup T, Hinrichsen EL, Grytten F, Echtermeyer A. Thermal conductivity of anisotropic, inhomogeneous high-density foam calculated from three-dimensional reconstruction of microtome images. J Appl Polym Sci 2013;130(2):1020–8. https://doi.org/10.1002/app.39238.

[16] EQUINOR. 2018. Online; accessed, https://www.equinor.com/.

[17] SHAWCOR. Thermotite; polypropylene insulation systems. 2018. Online; accessed, http://www.brederoshaw.com/non_html/pds/BrederoShaw_PDS_Thermotite.pdf.

[18] BOREALIS. Borcoat EA165E. 2019. Online; accessed, https://www.borealisgroup. com/product/borcoat-ea165e/.

[19] Johnsen J, Grytten F, Hopperstad OS, Clausen AH. Influence of strain rate and temperature on the mechanical behaviour of rubber-modified polypropylene and cross-linked polyethylene. Mech Mater 2017;114:40–56.

[20] BOREALIS BA202E. Online; accessed, https://www.borealisgroup.com/produc t/ba202e/; 2019.

[21] Als-Nielsen J, McMorrow D. Elements of modern X-ray physics. second ed. John Wiley & Sons, Ltd; 2011. ISBN 978-0-470-97394-3.

[22] Halary JL, Laupretre F, Monnerie L. Polymer materials: macroscopic properties and molecular interpretations. Wiley; May 2011. ISBN: 978-0-470-61619-2.

[23] Doroudiani S, Park CB, Kortschot MT. Effect of the crystallinity and morphology on the microcellular foam structure of semicrystalline polymers. Polym Eng Sci 1996; 36:21.

[24] Michaels AS, Bixler HJ. Flow of gases through polyethylene. J Polym Sci 1961;L: 413–39.

[25] Instron. 5980 floor model systems for high-capacity universal testing. Online; accessed August-2018, http://www.instron.us/en-us/products/testing-systems/un iversal-testing-systems/electromechanical/5900/5980-floor-model.

[26] Fagerholt E. eCorr digital image correlation. Online; accessed August-2018, https://www.ntnu.edu/kt/ecorr.

[27] Ulrich D, van Rietbergen B, Weinans H, Rüegsegger P. Finite element analysis of trabecular bone structure: a comparison of image-based meshing techniques. J Biomech 1998;31:1187–92. https://doi.org/10.1016/S0021-9290(98)00118-3.

[28] Tomasi C, Manduchi R. Bilateral filtering for gray and color images. In: Proceedings of the 1998 IEEE international conference on computer vision; 1998.

[29] Otsu N. A threshold selection method from gray-level histograms. IEEE Trans Syst Man Cybern B Cybern 1998;9(1):62–6. https://doi.org/10.1109/TSMC.1979. 4310076.

[30] Callister WD, Rethwisch DG. Materials science and engineering. eighth ed. John Wiley & Sons; 2011. ISBN 978-0-470-50586-1.

[31] Vieille B, Albouy W, Taleb L. About the influence of stamping on thermoplastic-based composites for aeronautical applications. Compos B Eng 2013;45:821–34.

[32] Dusunceli N, Colak OU. Modelling effects of degree of crystallinity on mechanical behavior of semicrystalline polymers. Int J Plast 2008;24:1224–42.

[33] Fischer F, Lim GT, Handge UA, Altstädt V. Numerical simulation of mechanical properties of cellular materials using computed tomography analysis. J Cell Plast 2009;45.